JGR Oceans

RESEARCH ARTICLE
10.1029/2020JC016521

**Key Points:**

- The energetics-based estimation of tidal mixing takes into account the contributions of both locally and remotely generated internal tides
- The internal tides in the western boundary island chain are the dominant energy sources for turbulent dissipation in the Andaman Sea (AS)
- Enhanced tidal dissipation and mixing are found in the deep basin of the AS and are much stronger than those in the Bay of Bengal

**Correspondence to:**
W. Yu and Z. Liu,
yuwd@mail.sysu.edu.cn;
zyliu@xmu.edu.cn

**Citation:**
Peng, S., Liao, J., Wang, X., Liu, Z., Liu, Y., Zhu, Y., et al. (2021). Energetics-based estimation of the diapycnal mixing induced by internal tides in the Andaman Sea. *Journal of Geophysical Research: Oceans*, *126*, e2020JC016521. https://doi.org/10.1029/2020JC016521

Received 17 JUN 2020
Accepted 26 FEB 2021

# Energetics-Based Estimation of the Diapycnal Mixing Induced by Internal Tides in the Andaman Sea

**Shiqiu Peng[1,2,3,4], Jiawen Liao[1,4,5], Xiaowei Wang[6], Zhiyu Liu[7], Yanliang Liu[2,8], Yuhang Zhu[1,3,4], Bingtian Li[9], Somkiat Khokiattiwong[10], and Weidong Yu[11,12,13]**

[1]State Key Laboratory of Tropical Oceanography, South China Sea Institute of Oceanology, Chinese Academy of Sciences, Guangzhou, China, [2]Laboratory for Regional Oceanography and Numerical Modeling, Qingdao National Laboratory for Marine Science and Technology, Qingdao, China, [3]Southern Marine Science and Engineering, Guangdong Laboratory (Guangzhou), Guangzhou, China, [4]University of Chinese Academy of Sciences, Beijing, China, [5]National Supercomputer Center in Guangzhou (Sun Yat-Sen University), Guangzhou, China, [6]Key Laboratory of Ocean Circulation and Waves, Institute of Oceanology, Chinese Academy of Sciences, Qingdao, China, [7]State Key Laboratory of Marine Environment Science, and Department of Physical Oceanography, College of Ocean and Earth Sciences, Xiamen University, Xiamen, China, [8]Center for Ocean and Climate Research, First Institute of Oceanology, Ministry of Natural Resources, Qingdao, China, [9]Department of Ocean Science and Engineering, Shandong University of Science and Technology, Qingdao, China, [10]Phuket Marine Biological Center, Phuket, Thailand, [11]School of Atmospheric Sciences, Sun Yat-Sen University, Zhuhai, China, [12]Key Laboratory of Tropical Atmosphere-Ocean System (Sun Yat-Sen University), Ministry of Education, Zhuhai, China, [13]Southern Marine Science and Engineering Guangdong Laboratory (Zhuhai), Zhuhai, China

**Abstract** The Andaman Sea (AS) is characterized by surprisingly weak stratification in its deep basin in drastic contrast to the nearby Bay of Bengal (BoB), presumably due to strong diapycnal mixing fertilized by the dissipation of internal tides. Here, we report on the first estimates of tidal mixing in the AS using idealized numerical simulations resolving the generation and evolution of low-mode internal tides. The estimation is based on a diagnostic analysis of the energetics of the simulated internal tides of both local and non-local origins. The results highlight the dominant role of the internal tides generated in the channels along the western boundary island chain in energizing diapycnal mixing in the entire AS. Tidal dissipation and mixing in the deep basin of the AS are found to be highly elevated, with the depth-integrated dissipation rate and the diapycnal diffusivity being $O(10^{-2}–10)$ W m$^{-2}$ and $O(10^{-3}–10^{-2})$ m$^2$ s$^{-1}$, respectively, both of which are 1–2 orders of magnitude larger than those in the deep BoB. These model-based estimates of tidal mixing are in general consistent with those from *in situ* conductivity-temperature-depth (CTD) measurements using the fine-scale parameterization. Our results suggest that the oft-used tidal mixing parameterization considering only local internal tide generation would underestimate the depth-integrated tidal dissipation in the AS by several orders of magnitude, highlighting therefore the necessity of considering contributions of non-local internal tides in parameterizing tidal dissipation and mixing in marginal seas like the AS.

**Plain Language Summary** The Andaman Sea (AS) is a marginal sea of the eastern Indian Ocean featured by strong internal tides, the dissipation of which can induce elevated turbulent mixing that tends to homogenize water properties at different depths. Hydrographic measurements suggest that the deep water in the AS is indeed rather well mixed, in drastic contrast to that in the nearby Bay of Bengal (BoB). Yet, knowledge on mixing characteristics in the AS remains very limited. To this end, we provide the first energetics-based estimation of internal-tide-induced turbulent dissipation and mixing in the AS using idealized numerical simulations resolving the generation and evolution of low-mode internal tides. Our main finding is that turbulent dissipation and mixing are elevated in the deep AS due to the dissipation of internal tides originated from the channels along the western boundary island chain. These model-based estimates are supported by the mixing estimates from *in situ* measurements, and suggest that turbulent mixing in the deep AS is larger than that in the deep BoB by 1–2 orders of magnitude. This provides a physical interpretation for the noted drastic contrast in the distribution of water properties in the AS and BoB.

## 1. Introduction

Diapycnal mixing plays an essential role in setting the global ocean stratification and in driving the meridional overturning circulation (MOC) (e.g., Marshall & Speer, 2012; Talley, 2013). It further exerts significant impacts on tracer distributions as well as local/global climate variability and change through diapycnal tranports of materials and heat (e.g., Johns et al., 2011; Kostov et al., 2014; Rahmstorf, 2003; Sanchez-Franks & Zhang, 2015). A canonical value of $10^{-4}$ $m^2$ $s^{-1}$ was estimated by Munk (1966) for the globally averaged diapycnal diffusivity to maintain the observed abyssal stratification. Subsequent observations suggest that diapycnal mixing is generally an order of magnitude weaker in the ocean interior over smooth topography (e.g., Ledwell et al., 1993); diapycnal mixing is, however, much elevated in regions with rough topography such as seamounts, ridges, canyons (e.g., Carter & Gregg, 2002; Ferron et al., 1998; Kunze & Toole, 1997; Ledwell et al., 2000; Polzin et al., 1997) and continental shelves in marginal seas (e.g., MacKinnon & Gregg, 2003). The enhanced diapycnal mixing at these hotspots results mainly from the dissipation of internal tides (i.e., internal waves with tidal frequencies, also called baroclinic tides) which are generated when barotropic tidal currents flow over rough topography (e.g., Niwa et al., 2004; Wang et al., 2016). The total energy generation of internal tides in the global ocean is estimated to be about 1 TW (Egbert & Ray, 2000), providing roughly half of the energy required to drive the global deep mixing (Munk & Wunsch, 1998).

Located to the east of the Bay of Bengal (hereinafter denoted as BoB), the Andaman Sea (AS) is a semi-enclosed marginal sea of the eastern Indian Ocean, connected with the BoB mainly through three major channels: the shallow Preparis Channel of depth around 250 m between south of Myanmar and north of the Andaman islands, the deep Ten Degree Channel of depth around 600 m between south of the Andaman islands and north of the Nicobar islands (specifically, the Car Nicobar island), and the deep Great Channel of depth around 1,500 m between south of the Nicobar islands (specifically, the great Nicobar island) and north of Sumatra (Figure 1). In addition, shallower and smaller channels also exist among the Nicobar Islands. The AS shares similarities with the South China Sea (SCS), a marginal sea of the North Pacific, in aspects of geographic latitudes, strong tidal forcing, rough/complex topography, and fully enclosed basin below a certain depth (AS with 1,500 m vs. SCS with 2,400 m), and thus it may host strong internal tides that could induce greatly enhanced turbulent dissipation and mixing as in the SCS (e.g., Niwa & Hibiya, 2011, 2014; Simmons, 2004; Wang et al., 2016). The AS is indeed known for its strong internal waves (e.g., Osborne & Burch, 1980). As shown in Figure 2, internal waves are clearly visible in synthetic aperture radar (SAR) images. Moreover, the profiles of potential temperature and dissolved oxygen along the 10°N transect from the WOCE data set show a nearly uniform distribution below 1,000 m, in dramatic contrast to the much more stratified water in the BoB, indicating strong diapycnal mixing in the AS (Figure 3).

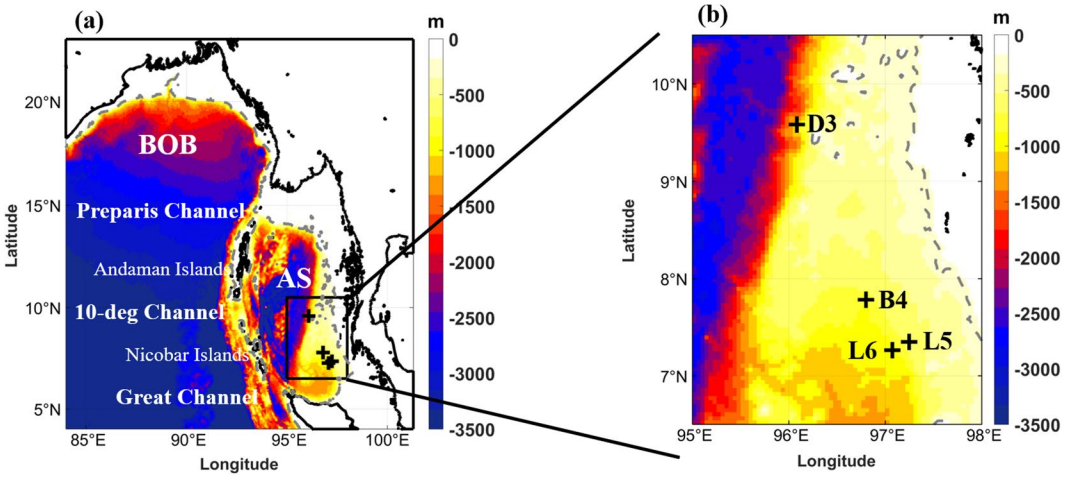


**Figure 1.** (a) The geography and bathymetry of the Andaman Sea (AS) and the eastern part of the Bay of Bengal (BoB), with (b) observation sites (denoted by cross) of temperature/salinity profiles enclosed by the rectangle area that is enlarged in the right panel. The black solid curve represents the coastline, and the gray dash contours denote the 200-m isobaths. The temperature/salinity profiles at these sites were obtained by conductivity-temperature-depth (CTD) downward casts during two cruises in November 2010 (L5, L6) and December 2018 (B4, D3), respectively.

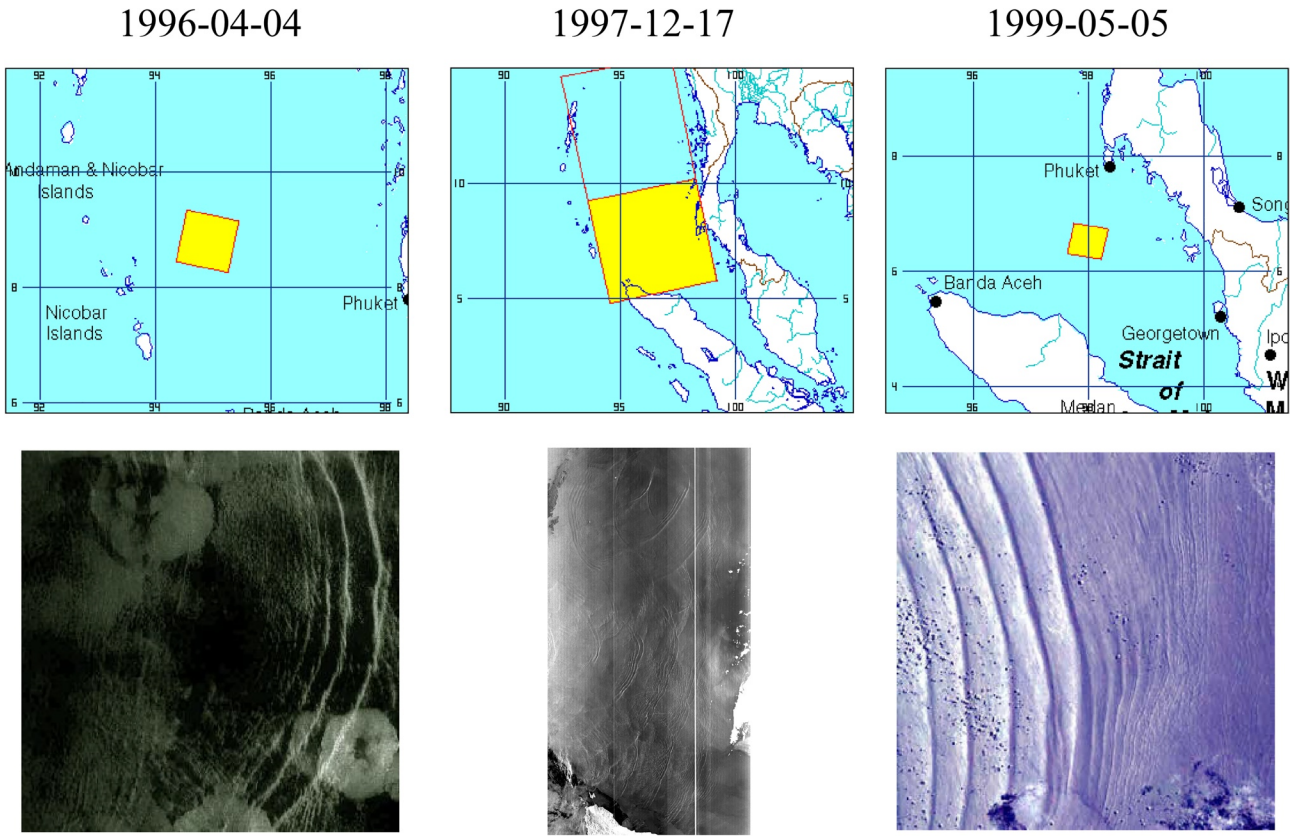


**Figure 2.** ERS-1/2 SAR images from The Centre for Remote Imaging, Sensing and Processing (CRISP) indicating internal waves in the AS (https://crisp.nus.edu.sg/~research/internal_waves/internal_waves.htm).

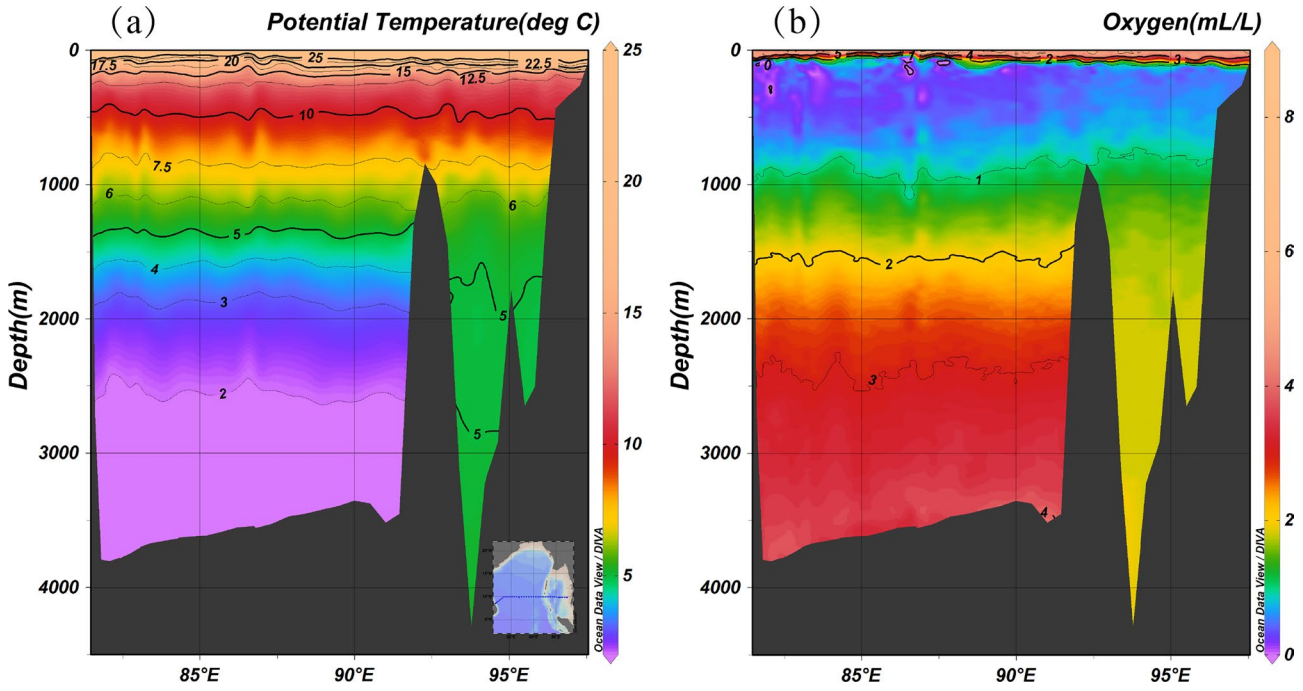


**Figure 3.** The vertical cross-sections of (a) potential temperature and (b) dissolved oxygen along 10°N from the WOCE data set.

However, due to a lack of observations in the AS, the regional characteristics of diapycnal mixing in the AS remain unknown, and the impacts of this mixing on water mass transformation, circulation, biogeochemistry, and ecosystem dynamics in the AS have yet to be revealed.

One way to quantify the diapycnal mixing induced by internal tides (hereinafter referred simply to as tidal mixing) is to perform a diagnostic analysis of the energetics of numerically simulated internal tides based on simulations that (at least) resolve the low-mode internal tides, as was done by Wang et al. (2016) for the SCS. Because the dissipation of internal tides of local and non-local origins are both considered, tidal mixing estimates as such appear to agree well with observational mixing estimates in the SCS. Most importantly, the estimates are found to be 1–2 orders of magnitude larger than those estimated from the oft-used tidal mixing parameterization of St Laurent et al. (2002) (hereinafter referred to as LSJ02), where only the dissipation of locally generated internal tides is considered. Given the similarities shared by the SCS and the AS, the same approach is adopted here to examine internal tide energetics in the AS, aiming at quantifying tidal mixing characteristics in the AS.

This paper is organized as follows. Section 2 reviews the methodology of the estimation of the turbulent kinetic energy dissipation rate and diapycnal diffusivity due to the dissipation of internal tides, followed by a description of the model setup in Section 3. Section 4 presents the energetics analysis of internal tides from tidal simulations. The estimates of turbulent dissipation and diapycnal diffusivity, as well as a validation against observational dissipation estimates with the fine-scale parameterization, are given in Section 5. Summary and discussion are included in the final part.

## 2. Methodology

The estimation of the turbulent kinetic energy dissipation rate and diapycnal diffusivity is based on an energy budget analysis of the simulated internal tides from idealized numerical simulations resolving low-mode internal tides (e.g., Kang & Fringer, 2012; Kelly et al., 2010; Nagai & Hibiya, 2015; Wang et al., 2016). As the method has been described in detail by Wang et al. (2016), here we only outline the main ideas. The energy budget analysis is based on the following relationship in which the tendency and advection terms are omitted as a first-order approximation:

$$\langle \mathrm{DIS}_{bc} \rangle \approx \langle \nabla_h \cdot F_{bc} \rangle - \langle E_{bt2bc} \rangle, \tag{1}$$

where the angle bracket represents a 14-day average to remove both the intra-tidal and spring-neap variabilities, $\mathrm{DIS}_{bc}$ is the depth-integrated energy dissipation rate of internal tides (more precisely, the loss of energy of the resolved low-mode internal tides), and $E_{bt2bc}$ and $\nabla_h \cdot F_{bc}$ are the depth-integrated barotropic-to-baroclinic tidal energy conversion rate and the divergence of the depth-integrated energy flux of internal tides, respectively:

$$E_{bt2bc} = g \int_{-H}^{\eta} \rho' w_{bt} dz, \tag{2}$$

$$\nabla_h \cdot F_{bc} = \nabla_h \cdot \left( \int_{-H}^{\eta} u' \mathrm{p}' dz \right), \tag{3}$$

where $\rho'$ and $P'$ are the perturbations of density and pressure, respectively, $u'$ is the velocity of internal tides, and $w_{bt}$ the vertical velocity associated with barotropic tides. $H$ and $\eta$ represent the time-mean water depth and surface tidal elevation, respectively. Following Nash et al. (2005), the pressure perturbations are calculated from the density perturbation $\rho'$ using the following equation:

$$p'(z,t) = -\frac{1}{H} \int_{-H}^{\eta} \int_{z}^{\eta} g\rho'(\hat{z},t) d\hat{z} dz + \int_{z}^{\eta} g\rho'(\hat{z},t) d\hat{z}. \tag{4}$$

Once the depth-integrated energy dissipation rate is obtained, the diapycnal diffusivity is estimated following Osborn (1980):

$$k_v = \frac{\Gamma \langle \mathrm{DIS}_{bc} \rangle F(z)}{\rho N^2}, \tag{5}$$

where $\rho$ and $N^2$ are the density of seawater and the squared buoyancy frequency, respectively, which are calculated from the annual mean climatology of GDEMv3 data that are also used as the initial stratification in our simulations. Here, we have assumed that the energy lost from the resolved low-mode internal tides is eventually transferred to the small-scale turbulence generating diapycnal mixing.

In Equation 5, $\Gamma$ is the mixing efficiency, which can be parameterized as follows according to Mashayek et al. (2017):

$$\Gamma(Re_b) = \frac{2\Gamma^* \left( \frac{Re_b}{Re_b^*} \right)^{\frac{1}{2}}}{1 + \left( \frac{Re_b}{Re_b^*} \right)}, \tag{6}$$

where $Re_b = \frac{\langle \mathrm{DIS}_{bc} \rangle F(z)}{\nu \rho N^2}$ is the buoyancy Reynolds number characterizing the intensity of stratified turbulence. Here, $\Gamma^*$ is the maximum value of the mixing efficiency at $Re_b = Re_b^*$. We have set $\Gamma^*$ and $Re_b^*$ to be 0.2 and 100, respectively, adopting the lower bounds of Mashayek et al. (2017). $F(z)$ is a vertical structure function to describe vertical distribution of the energy dissipation. Following St Laurent et al. (2002) and assuming that the dissipation of internal tides of both local and non-local origins to be bottom-intensified and exponentially decay away from the seafloor, $F(z)$ is formulated as follows:

$$F(z) = \frac{\exp\left(-(D+z)/\zeta\right)}{\zeta\left(1 - \exp\left(-D/\zeta\right)\right)}, \tag{7}$$

where $\zeta$ is the vertical decay scale and is set to be the same as in St Laurent et al. (2002), that is, $\zeta = 500$ m, and $D$ is the total water depth.

It is worthwhile noting that the main difference between LSJ02 and the scheme based on the internal tide energetics analysis is how the generation and dissipation of internal tides are estimated. In addition to considering the dissipation of locally generated internal tides, the latter also takes the dissipation of non-locally generated internal tides into account. Therefore, the scheme employed in this study is expected to be more realistic in characterizing tidal mixing properties in semi-enclosed marginal seas with rough/complex topography and channels connecting with the open ocean, such as the SCS and the AS. As shown by Wang et al. (2016), the estimates of diapycnal diffusivity in the SCS using this scheme are generally consistent with those from microstructure measurements and fine-scale parameterizations, and are 1–2 orders of magnitude larger than those from LSJ02 in most regions of the basin. Moreover, a constant mixing efficiency $\Gamma = 0.2$ was used in LSJ02 as well as many previous studies including Wang et al. (2016), while this study employs a variable $\Gamma$ which depends on the buoyancy Reynolds number and has an upper limit value of 0.2. Although Gregg et al. (2018) argued that the canonical value of 0.2 is within observational accuracy, there are studies showing that the mixing efficiency is well below 0.2 when the stratification is very weak and thus the adoption of $\Gamma = 0.2$ generally results in an overestimate of the diapycnal mixing in the deep ocean (Mashayek et al., 2017). The sensitivity of the estimated diffusivities to the mixing efficiency $\Gamma$ as well as the associated parameters $\Gamma^*$ and $Re_b^*$ in Equation 5 is presented in Appendix A. Although the parameterization of $\Gamma$ by Mashayek et al. (2017) is a valuable step forward, it is well understood that $\Gamma$ cannot really be determined by $Re_b$ alone (e.g., Monismith et al., 2018; Salehipour et al., 2016; Scotti & White, 2016). In fact, the parametric dependence of the mixing efficiency remains a hot topic of debate in the community.

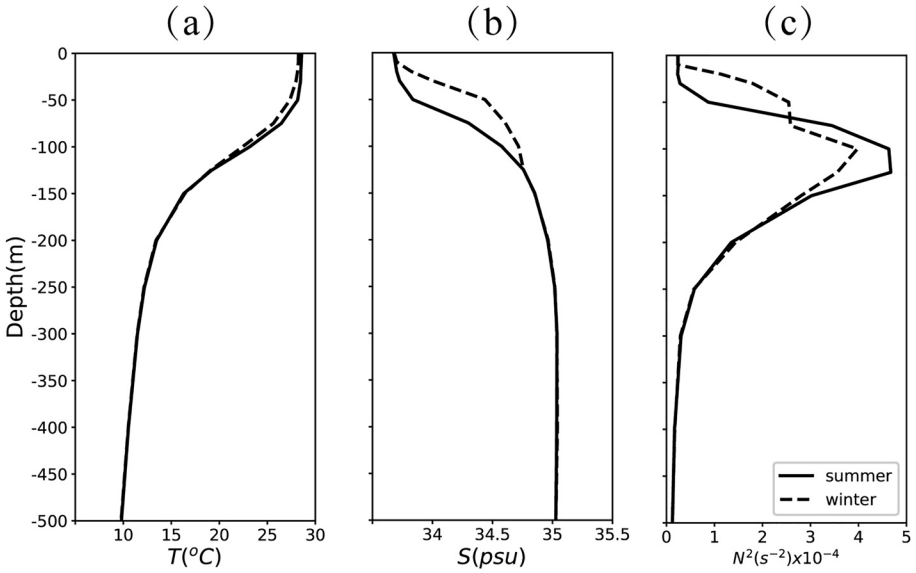


**Figure 4.** Vertical profiles of the monthly mean climatology of (a) potential temperature ($T$), (b) salinity ($S$), and (c) the corresponding squared buoyancy frequency ($N^2$) from the GDEMv3 data which are used as the initial fields in winter (dashed lines) and summer (solid lines) runs.

## 3. Model Configuration

The Massachusetts Institute of Technology General Circulation Model (MITgcm) (Marshall et al., 1997) in hydrostatic mode is employed to simulate internal tides in the AS. This model is structured in $z$ coordinates, and the GMRedi parameterization (Gent-McWilliams/Redi SGS Eddy Parameterization) is used to remove unrealistic diapycnal mixing introduced by the advection scheme (third-order discrete space and time flux limiter scheme) in $z$-coordinate. This model has been widely used in physical oceanography, including simulations of the generation, propagation, and dissipation of internal tides over rough topography (e.g., Buijsman et al., 2012, 2014; Klymak et al., 2016; Wang et al., 2016). Our model domain covers the entire AS as well as the eastern part of the BoB, from 4°N to 24°N, and 84°E to 102°E, with a grid spacing of 1/24°×1/24° (~5 km) over the entire domain and high resolution 30 arc-second bathymetry from the GEBCO_14 data (http://www.gebco.net/) (Figure 1a). Fifty-eight $z$-levels are set in the vertical direction, which have thicknesses of 10–50 m for the top 12 levels from the surface to a depth of 300 m, 100 m for the following 46 levels. As shown in Appendix B, the current model setup regarding these horizontal and vertical resolutions provides an acceptable resolution of the low-mode internal tides and thus is adopted with the consideration of computing-resource saving.

To simulate internal tides, horizontally uniform but vertically stratified temperature and salinity fields are used as the model initial conditions, which are the same as the temperature and salinity profiles derived from the monthly mean climatology of GDEMv3 (http://www.usgodae.org/pub/outgoing/static/ocn/gdem/) at the site (92.5°E, 5.5°N) that has the largest water depth in the simulated region (Figure 4). As shown in Figure 4, small differences of the stratification between the winter (January) and summer (July) seasons in the upper 500 m (Figure 4) exist. To obtain a climatological tidal mixing estimate, simulations are performed for each of the two seasons using the corresponding stratification, and then the mean of the two seasons is taken as the annual mean climatology.

The semi-diurnal barotropic tides are the dominant tidal constituents in the BoB (e.g., Murty & Henry, 1983). According to the results from our barotropic-tide model, the energy of semi-diurnal barotropic tides (including $M_2$ and $S_2$) can account for 96% of the total barotropic-tide energy in the AS, which is the main energy source of the internal tides in the basin. Therefore, the semi-diurnal tidal constituents ($M_2$, $S_2$) with their amplitudes and phases extracted from the Oregon State University inverse barotropic tidal model (OTIS) (Egbert & Erofeeva, 2002; Egbert et al., 1994) with 1/30° spatial resolution (http://volkov.oce.orst.edu/tides/YS.html) are used to force the model at the open boundaries where a 0.5°-wide sponge layer

**Table 1**
*The Observational Data and Model Results at Four Tidal Gauges*

| | | Station | | | | | | | |
|---|---|---|---|---|---|---|---|---|---|
| | | Chittagong | | Sittwe | | Moulmein | | Sabang | |
| | | (91.83°E, 22.33°N) | | (92.90°E, 20.15°N) | | (97.62°E, 16.48°N) | | (95.33°E, 5.83°N) | |
| Tide type | | Am (m) | Ph (°) | Am (m) | Ph (°) | Am (m) | Ph (°) | Am (m) | Ph (°) |
| $M_2$ | Obs | 1.58 | 134.11 | 0.69 | 297.40 | 1.00 | 147.17 | 0.43 | 55.81 |
| | Model | 1.31 | 133.84 | 0.69 | 259.42 | 1.20 | 170.10 | 0.43 | 55.69 |
| | Error | 17.09% | 0.20% | 0.00% | 12.77% | 20.00% | 15.58% | 0.00% | 0.22% |
| $S_2$ | Obs | 0.64 | 155.58 | 0.4 | 297.63 | 0.47 | 146.74 | 0.39 | 110.92 |
| | Model | 0.50 | 155.59 | 0.4 | 282.37 | 0.50 | 209.13 | 0.30 | 110.92 |
| | Error | 21.88% | 0.00% | 0.00% | 5.13% | 6.38% | 42.52% | 23.08% | 0.00% |

is imposed to remove artificial reflections. Following Wang et al. (2016), no turbulence closure is adopted in the simulations to simplify the related analysis; the horizontal and vertical diffusivities are set to zero ($K_h = K_v = 0$, i.e., ignoring the diffusion of temperature and salinity), while the horizontal viscosity, vertical viscosity, and bottom drag coefficient are specified uniformly throughout the domain as $A_h = 0.01$ m$^2$ s$^{-1}$, $A_v = 1 \times 10^{-5}$ m$^2$ s$^{-1}$, and $C_d = 2.5 \times 10^{-3}$, respectively. As validated by Wang et al. (2016) through a set of sensitivity experiments, the values of viscosity and bottom drag coefficient do not significantly influence the internal tide energy budget.

For each simulation, the model is integrated from a cold start (i.e., a state of rest) for 14 days to cover a spring-neap tidal cycle, starting from January 14, 2011 and July 10, 2011 for the winter and the summer, respectively. For each season, hourly model output during the 14-day spring-neap tidal cycle is used for the energy budget analysis.

## 4. Energy Budget of Internal Tides

In order to validate our model results, we first extract the barotropic tides of $M_2$ and $S_2$ from the simulations and compare their amplitudes (phases) against those from tide gauges, as presented in Table 1. Due to coastal runoff, there is some deviation of amplitude and phase between the observation and model simulation at Chitagong, Sittwe, and Moulmein, but the observed amplitudes and phases of the Sabang with little influence of runoff are in great agreement with the model results.

Figure 5 shows the barotropic tidal energy fluxes from model simulations, calculated by $\mathbf{P} = \rho g h \langle u_{bt} \eta \rangle$, for the two semi-diurnal tidal constituents ($M_2$, $S_2$). The patterns are close to those of OTIS, although the simulated amplitudes are somewhat different (not shown), probably due to the use of different topography atlases. It is evident that the barotropic tidal energy enters the AS from the BoB through the three major channels, that is, north of the Andaman islands, between the Andaman islands and the Nicobar islands, and north of Sumatra, and converges in the middle of the northern AS basin. The barotropic tidal energy fluxes for $M_2$ ($S_2$) across the three channels are about 6.09 GW (1.68 GW), 5.55 GW (1.67 GW), and 9.66 GW (2.32 GW), respectively.

Figure 6 shows the spatial–temporal distributions of the near-surface pressure perturbations and the velocity of internal tides from the simulation forced by the two primary tidal constituents $M_2$ and $S_2$ in summer. The spatial distributions of the near-surface pressure perturbations calculated by Equation 4 demonstrate that strong internal tides are mainly generated in the three main channels and propagate eastward and westward into the AS and the BoB, respectively, with larger amplitudes during the spring tide than during the neap tide. The eastward-propagating internal tides cross the AS and reach the continental slope of the eastern AS basin, where they are mainly confined in regions deeper than 200 m. These features of the spatial distribution and propagation of the internal tides in the AS are generally consistent with the results of Mohanty et al. (2018). The internal tidal currents are found to be strongest in the near surface and feature

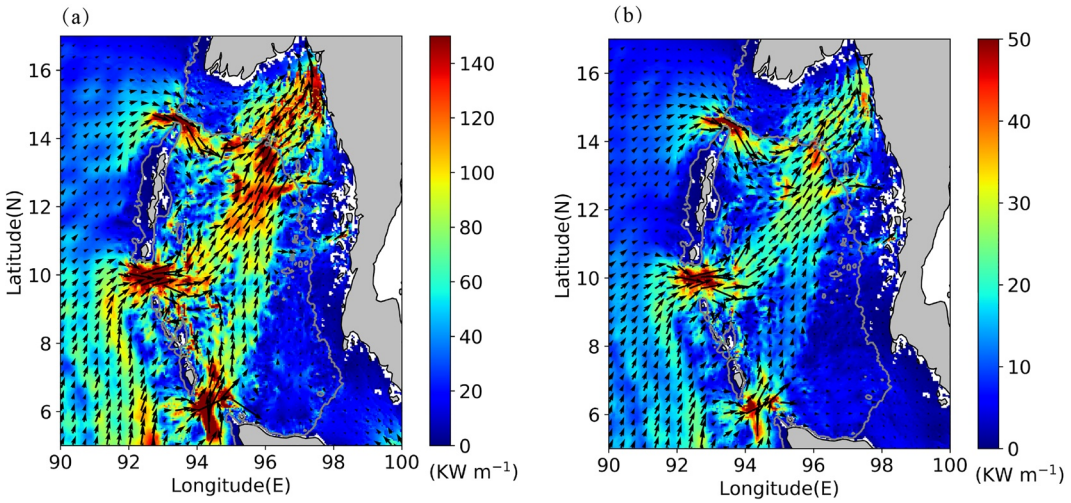


**Figure 5.** Barotropic tidal energy flux (vector) and its magnitude (color shading) for the semidiurnal tidal constituents (a) $M_2$ and (b) $S_2$. The gray contour denotes the 200-m isobath.

near-bottom intensification (Figure 6), which are similar to that in observations and model simulations for the SCS (e.g., Duda & Rainville, 2008; Klymak et al., 2011; Wang et al., 2016). It is also evident that internal tidal currents are stronger in the AS than in the BoB. Similar results (not shown) are seen in winter due to the similar stratification (Figure 4).

The depth-integrated barotropic-to-baroclinic tidal energy conversion and energy flux of internal tides as well as its divergence in the AS and the surrounding regions are shown in Figure 7. Positive (negative) values of the energy conversion imply the energy transfer from barotropic (baroclinic) tides to baroclinic (barotropic) tides. Negative conversion is attributed to the alteration of the phase of density perturbation by non-locally generated internal tides that could result in large phase differences (greater than 90°) between the density perturbation and the barotropic vertical velocity (Zilberman et al., 2009), implying multiple sources (Carter et al., 2012). Large positive energy conversion occurs in the regions of the three channels where rough topography exists, especially in the middle channel where the maximum value reaches 12.6 W m$^{-2}$, indicating that the internal tides are mainly generated in these regions; the generated internal tide energy radiates eastward into the AS and westward into the BoB, as indicated by the energy flux vectors of internal tides in Figure 7b. Negative values of energy conversion are seen in the AS and the BoB, implying the influence of non-locally generated internal tides on the local energy budget. While the maximum barotropic energy flux is found in the Ten Degree Channel (Figure 5), the maximum energy flux of internal tides occurs in the small channel between the center and north of the Nicobar islands (Figure 7b), suggesting the important role of rough topography around the small islands in shaping the energy flux of internal tides. The spatial distribution of the divergence of energy flux of internal tides has a similar pattern as that of barotropic-to-baroclinic tidal conversion, especially in the BoB; large positive values are seen in the three channels while negative values dominate in the AS basin, suggesting that the three channels are the main source regions of internal tide energy while the AS is the sink region.

To further investigate and quantify the source and sink of the internal tide energy in the AS basin and the western boundary island chain, an energy budget analysis of internal tides is performed for three western boundary regions (denoted as A, B, and C) from north to south which cover respectively the three major channels (region B also includes all the small channels among the Nicobar islands), and the AS interior (denoted as D), as shown by the dash rectangles in Figure 7a. Moreover, an additional region for the shelf area (< 200 m) in the AS is included. The results for the summer season are presented in Table 2. It can be seen that the three small western boundary regions are the main source regions of internal tide energy generation with a total barotropic-to-baroclinic conversion rate of about 17.57 GW which is three times larger than that for the large AS interior (i.e., region D); about half (~8.83 GW) of the energy converted to internal tides

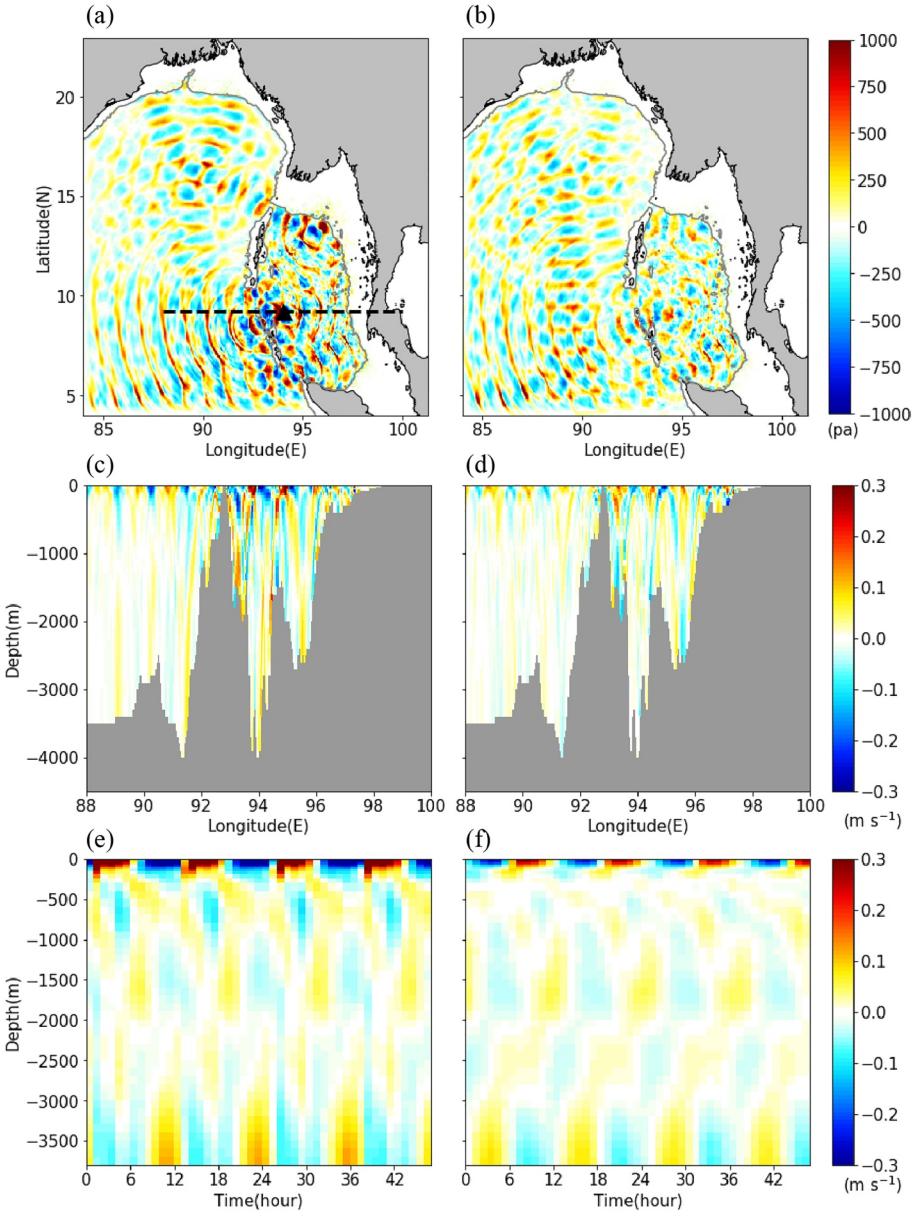


**Figure 6.** (a and b) Instantaneous near-surface pressure perturbation; (c and d) zonal velocity of internal tides along 9.2°N; and (e and f) the time variation of the zonal velocity of internal tides at site (9.2°N, 94°E) during the spring (left) and neap (right) tides in summer. The gray contours in Figure 6a and 6b denote the 200-m isobaths. The dark dash line and the black triangle in Figure 6a denote the section along 9.2°N and the site at 9.2°N and 94°E, respectively.

is dissipated locally, while the rest (8.74 GW) radiates away (i.e., eastward into the AS and westward into the BoB with positive energy flux divergence). The negative energy flux divergence (∼- 4.09 GW) indicates that the AS interior is a tidal energy sink, the magnitudes of which is comparable to the barotropic-to-baroclinic conversion rate (∼5.52 GW), providing nearly half of the total dissipation rate (∼9.61 GW) in the AS interior. Among the three western boundary regions (A, B, and C), region B has the largest energy conversion rate, energy flux divergence and energy dissipation rate with tidal mean values of ∼11.03, 5.47, and 5.56 GW, respectively. For the shelf area (< 200 m), the tidal mean conversion rate, energy flux divergence and dissipation rate are about 1.16, −0.73, and 1.89 GW, respectively. Similar results are obtained for the winter, as shown in Table 3.

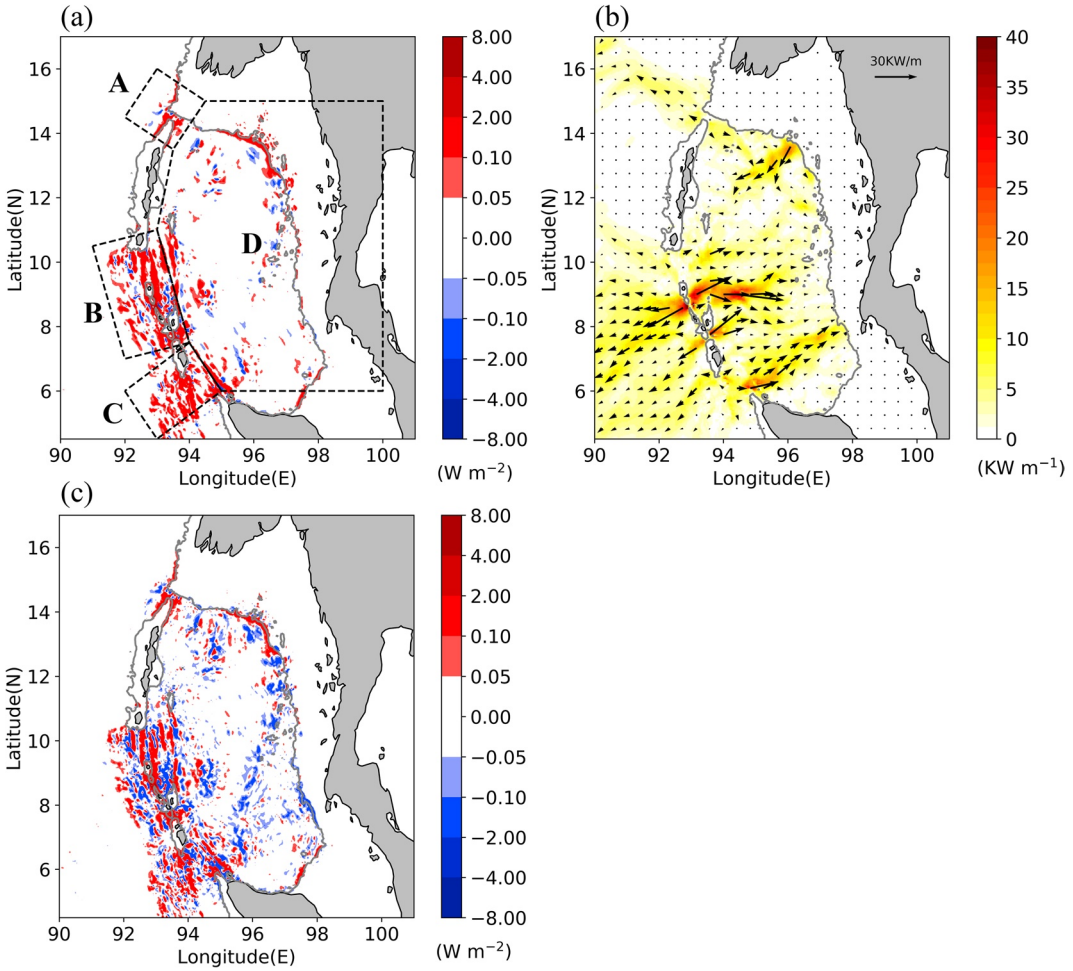


**Figure 7.** Depth-integrated (a) barotropic-to-baroclinic tidal energy conversion, (b) internal tide energy flux vector, and (c) internal tide energy flux divergence during the spring tide in summer. The gray contours denote the 200-m isobaths. A, B, C, and D in (a) denote the three regions along the western boundary island chain and the AS interior, respectively, used for the energy budget of internal tides analysis shown in Tables 2 and 3.

## 5. Estimation and Validation of Tidal Dissipation and Mixing

Figure 8a shows the annual-mean depth-integrated dissipation rate of internal tides by taking the average of the summer and winter seasons' results based on Equations 1–3. Large depth-integrated dissipation rates of about $O(10^{-2}$–$10)$ W m$^{-2}$ are found in the regions of the AS including the three major channels. This is about 1–2 orders of magnitude larger than that in the BoB. In particular, strong tidal dissipation occurs along the western island chain (especially in the middle and southern channels) and the eastern continental slope near the 200-m isobaths where rough topography exists, with the maximum dissipation rate being 0.90 W m$^{-2}$. This could be due to the different features in the size, depth, and topography of the two basins which influences the propagation and dissipation of the internal tides generated along the western boundary island chain: the BoB has a much wider basin with deeper and relatively smoother bottom bathymetry, which facilitates the westward propagating internal tides to travel far away in the BoB before being dissipated, whereas the eastward propagating internal tides may be reflected and confined in the AS basin on arriving at the shelf break, and finally get dissipated in the basin. Compared to the estimate of depth-integrated dissipation rates using LSJ02 which only considers

**Table 2**
*The Energy Budget of Internal Tides for the Three Regions (A, B, and C) Along the Western Boundary Island Chain and the AS Interior (D) As Well As the Shelf Area (< 200 m) in Summer*

| | A | B | C | D | <200 m |
|---|---|---|---|---|---|
| Conv | 1.414 | 11.028 | 5.123 | 5.517 | 1.157 |
| DivF | 1.000 | 5.473 | 2.266 | −4.092 | −0.728 |
| Diss | 0.414 | 5.555 | 2.857 | 9.609 | 1.885 |

*Note*. The Conv, DivF, and Diss denote the area-integrated conversion rate with a tidal period mean from barotropic to baroclinic tidal energy, divergence of internal tide energy flux, and dissipation rate of the internal tide energy (units: GW), respectively.

**Table 3**
*Same as Figure 2, but for Winter*

| | A | B | C | D | <200 m |
|---|---|---|---|---|---|
| Conv | 1.461 | 10.577 | 5.206 | 5.176 | 1.180 |
| DivF | 0.968 | 5.107 | 2.378 | −3.967 | −0.521 |
| Diss | 0.493 | 5.470 | 2.828 | 9.143 | 1.701 |

the dissipation of the locally generated internal tides (Figure 8b), the estimate based on the energy budget, which includes the dissipation of both the locally and non-locally generated internal tides, is about 2–4 orders of magnitude larger in both the AS basin and the BoB.

Given the depth-integrated dissipation rate of internal tides, the diapycnal diffusivity is obtained according to Equation 5 with a vertical decay scale of 500 m. Figure 9 shows the cross-section distributions of the dissipation rate and the diapycnal diffusivity along 9.2°N and 95°, respectively. Elevated dissipation rates of $O(10^{-7}–10^{-6})$ W kg$^{-1}$ are found over the rough topography, especially over ridges and along the shelf break, while enhanced mixing with diapycnal diffusivities of $O(10^{-3}–10^{-2})$ m$^2$ s$^{-1}$ occurs near the bottom of the entire AS basin. The diapycnal diffusivities in the deep BoB are generally 1–2 orders of magnitude smaller than those in the deep AS basin along 9.2°N (Figure 9b), which can be attributed to lower dissipation rates and larger buoyancy frequency in the deep BoB. The estimates of the dissipation rate and diapycnal diffusivities using LSJ02, as shown in Figure 10, are 1–2 orders of magnitude smaller than the above results based on the internal tide energy budget analysis which considers the energy dissipation of both the locally and non-locally generated internal tides.

The fine-scale parameterization of turbulence (e.g., Kunze et al., 2006) estimates turbulent dissipation and diapycnal mixing from the shear and strain induced by internal waves at the $O$(10–100 m) vertical scale. To validate the above model-based estimation by the energy budget analysis of internal tides, the fine-scale parameterization is adopted to estimate the turbulent kinetic energy dissipation rate using *in situ* observations of temperature and salinity profiles, which were obtained by conductivity-temperature-depth (CTD) casts during two cruises in the AS in November 2010 and December 2018. Considering that the fine-scale parameterization is not expected to work well in the near-field of internal tide generation as well as in the pycnocline (e.g., Jing et al., 2011; Kunze et al., 2006; Liu et al., 2017; Polzin et al., 2014), four observation sites are selected for the validation which are located on the eastern continental slope of the AS with water depth larger than 200 m (see Figure 1b), and the validation is made only beneath 200-m depth. It is found that the squared buoyancy frequency $N^2$ calculated from the numerical simulation matches that from the observed temperature/salinity ($T/S$) profiles very well (Figure 11). Except for station D3, the depth-integrated dissipation rates estimated by the energy budget analysis of internal tides are close to those estimated from the observed $T/S$ profiles using the fine-scale parameterization (Figure 12). Although uncertainties exist in the estimates using the fine-scale parameterization (e.g., Hibiya et al., 2012; Liu et al., 2017; Polzin et al., 2014), the above results provide a useful reference which suggests the reliability of the energetics-based estimates and the necessity of taking dissipation of non-locally generated internal tides into account.

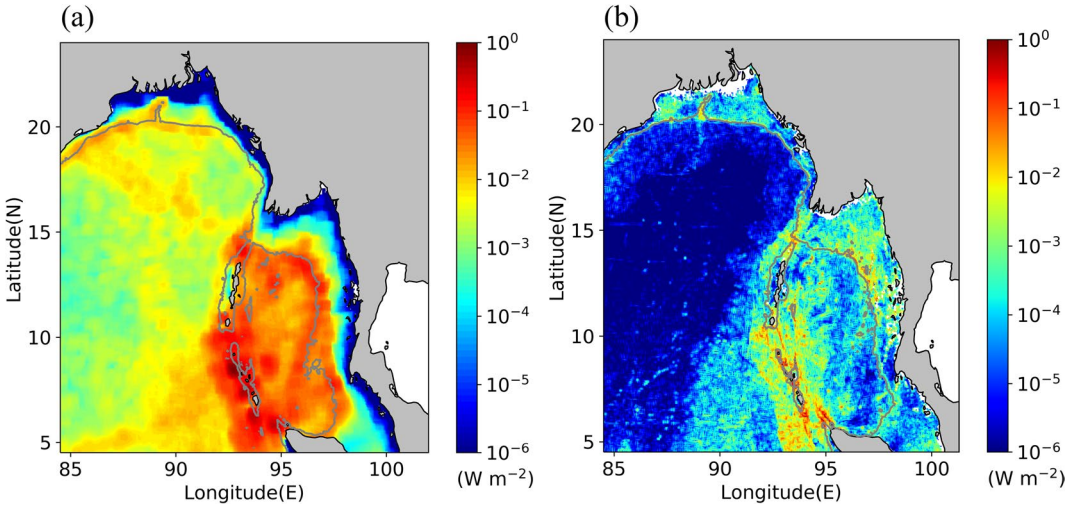


**Figure 8.** Annual-mean depth-integrated dissipation rate of internal tide energy estimated by (a) the internal tide model and energy budget analysis as well as (b) the LSJ02 parameterization. The gray contours denote the 200-m isobaths.

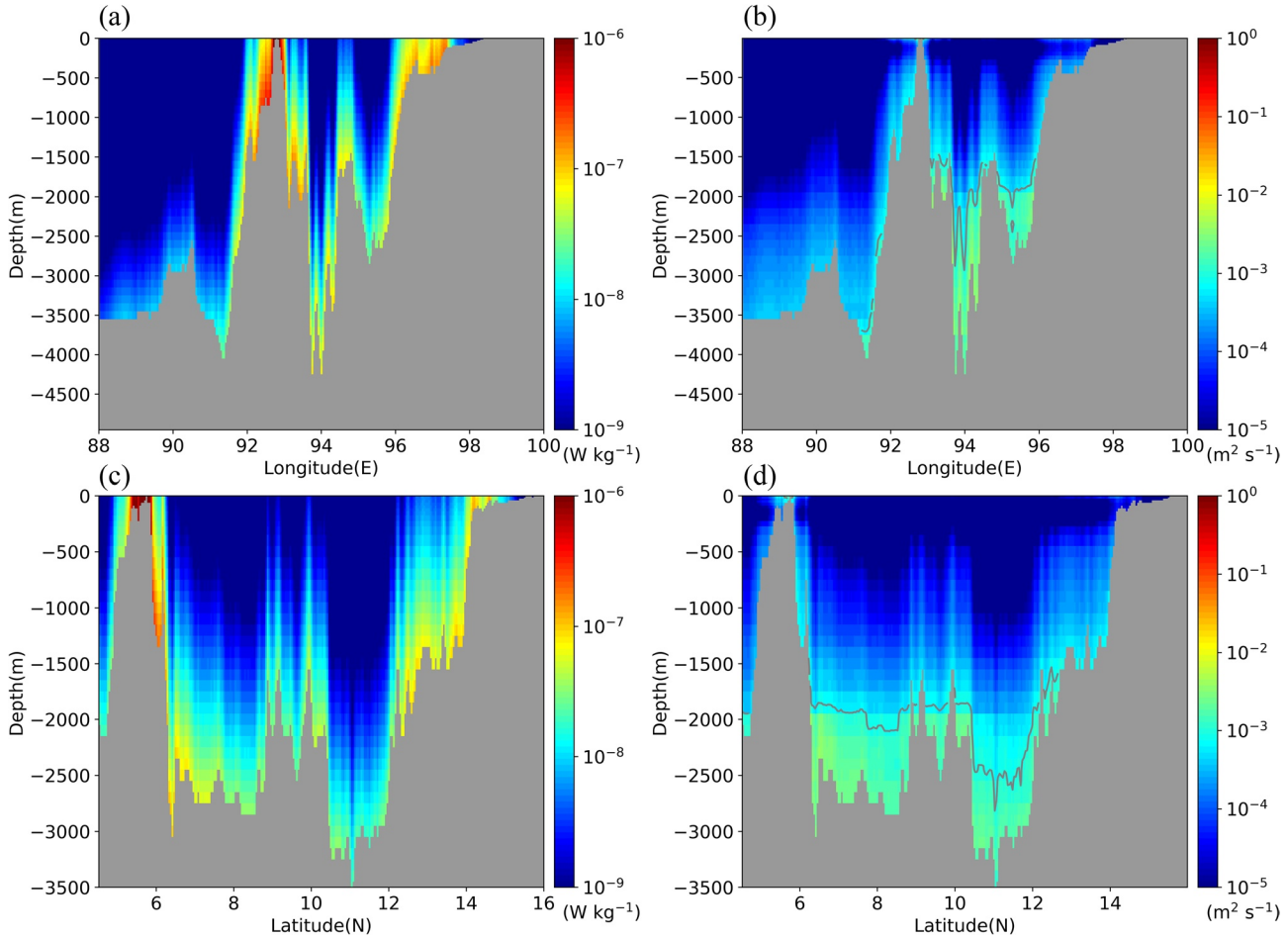


**Figure 9.** Cross-sectional distributions of (a and c) dissipation rate and (b and d) diapycnal diffusivity along (top) 9.2°N and (bottom) 95°E in the AS estimated by the internal tide model and energy budget analysis. The gray contour in (b) and (d) represents the value of $10^{-3}$ m$^2$ s$^{-1}$.

## 6. Summary and Discussion

In this study, a high-resolution configuration of the MITgcm resolving low-mode internal tides is implemented to simulate internal tides in the AS. An energy budget analysis of the internal tides is then employed to estimate tidal dissipation and mixing in the AS. Our key findings are as follows:

1) The semi-diurnal barotropic tides ($M_2$, $S_2$) account for 96% of the total barotropic-tide energy in the AS. The barotropic tidal energy enters the AS from the BoB through the three channels along the western boundary island chain, and converges in the middle of the northern AS basin, with energy fluxes for $M_2$ ($S_2$) across the three channels being about 6.09 GW (1.68 GW), 5.55 GW (1.67 GW), and 9.66 GW (2.32 GW), respectively.
2) Strong internal tides of primarily semi-diurnal frequencies are mainly generated in the channels or straits along the western boundary island chain and propagate respectively eastward into the AS and westward into the BoB, with larger amplitudes in spring tides than in neap tides. The internal tidal currents are found to be stronger in the AS than in the BoB.
3) Energy budget analysis reveals that the channels or straits along the western boundary island chain are the main source regions of internal tide energy with an annual mean total barotropic-to-baroclinic tidal energy conversion of about 17.6 GW; this energy is fluxed, in roughly equal amounts, eastward into the AS and westward into the BoB. In contrast, the AS interior is a sink, that is, the total tidal dissipation (~9.61 GW) greatly exceeds the local energy conversion (~5.52 GW), the overspending of which is supplied by non-locally generated internal tides (~4.09 GW). Enhanced tidal dissipation occurs over rough topography, especially over ridges and the shelf break, in the AS basin and along the western boundary

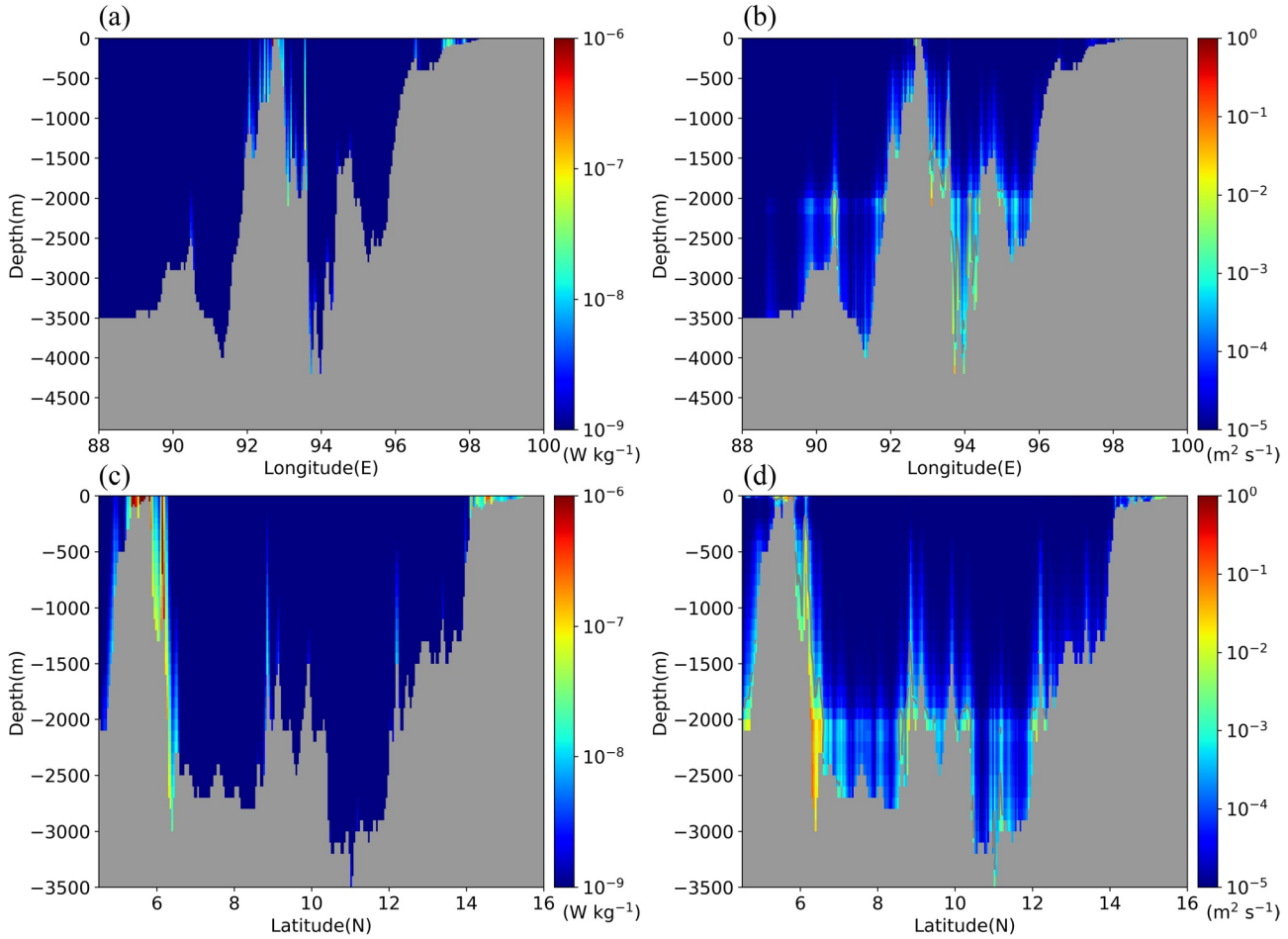


**Figure 10.** The same as Figure 9, but estimated by LSJ02 parameterization.

island chain with depth-integrated dissipation rate reaching to $O(10^{-1}$–$10)$ W m$^{-2}$, which is generally an order of magnitude larger than those in the BoB.

4) Elevated tidal dissipation with a depth-integrated dissipation rate of $O(10^{-2}$–$10)$ W m$^{-2}$ occurs in the AS deep basin and along the western boundary island chain, where the topography is complex. Based on the assumption of bottom-intensified tidal dissipation with a 500-m vertical decay scale, a three-dimensional mean field of the diapycnal diffusivity is obtained, from which enhanced tidal mixing with diapycnal diffusivities of $O(10^{-3}$–$10^{-2})$ m$^2$ s$^{-1}$ is found near the bottom of the entire AS basin. In comparison, the estimated depth-integrated dissipation rates and diapycnal diffusivities based on the energy budget analysis are about 2–4 and 1–2 orders of magnitude larger than those by LSJ02, respectively. This model-based estimation of the dissipation rate is generally in agreement with the estimation based on the fine-scale parameterization of turbulence using *in situ* observations at several locations on the eastern continental slope of the AS. This reaffirms the conclusion of Wang et al. (2016) that the estimation of tidal dissipation and mixing in marginal seas should consider the contribution of non-locally generated internal tides in addition to locally generated internal tides.
5) The estimated depth-integrated dissipation rates and diapycnal diffusivities of $O(10^{-3}$–$10^{-2})$ W m$^{-2}$ and $O(10^{-5}$–$10^{-3})$ m$^2$ s$^{-1}$ in the deep BoB are about 1–2 orders of magnitude lower than those in the deep AS, leading to the drastic contrast in the vertical distribution of potential temperature, salinity, and oxygen (as well as presumably other properties) between the two basins. Due to the BoB's much wider basin with deep and relatively smooth bottom bathymetry, the westward propagating internal tides generated along the western boundary island chain may travel far away in the BoB before being dissipated, whereas

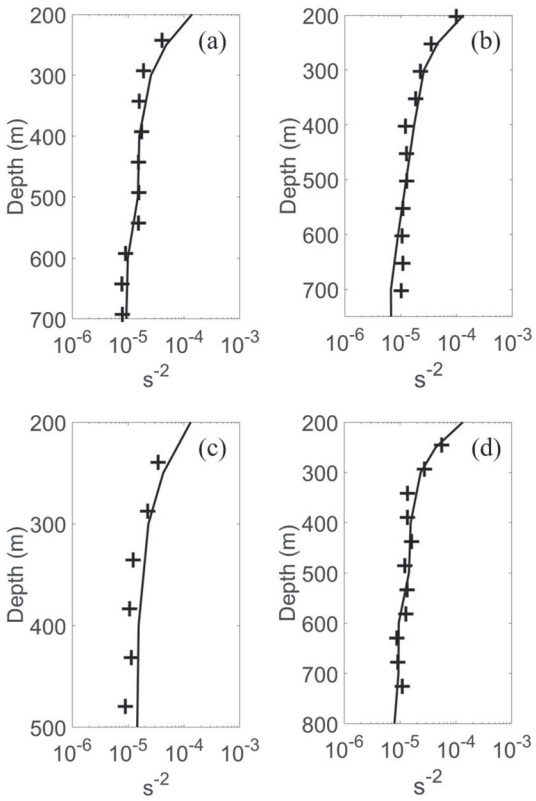


**Figure 11.** The squared buoyancy frequency $N^2$ calculated from model output (solid line) and *in situ* observations (cross) at sites of (a) B4, (b) D3, (c) L5, and (d) L6 (see Figure 1 for the geographic locations of the sites).

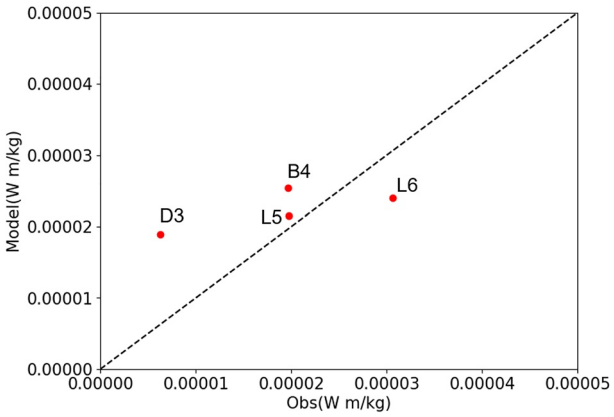


**Figure 12.** The depth-integrated dissipations at the four sites estimated by the energy budget analysis of the model simulated internal tides and by the fine-scale parameterization of turbulence from observed temperature/salinity profiles (see Figure 1 for the geographic locations of the sites).

the eastward propagating internal tides may be reflected on arriving at the shelf break and are confined in the AS basin, and finally get dissipated in the basin.

Although the energetics-based method could be a promising way to include the contributions from both locally and non-locally generated internal tides, the estimation in this study is based on some simplifications, that is, horizontally uniform stratification, no background ocean circulations, etc., and on the assumption that the dissipation of the locally and non-locally generated internal tides are both bottom-enhanced with a vertical decay scale of 500 m. In the real ocean, the stratification varies both temporally and spatially, and background ocean circulations of various scales exist all the time, which could exert significant influence on internal tides including their generation, propagation, and dissipation (e.g., Jan et al., 2012; Kerry et al., 2013, 2014). Meanwhile, the assumption of bottom-enhanced and exponentially decayed dissipation of both locally and non-locally generated internal tides, especially the choice of a 500-m vertical decay scale, is empirical and lacks full validation for its applicability in different regions. Therefore, considerable uncertainties exist in the estimates of tidal dissipation and mixing presented in this study, which could be reduced by employing more realistic ocean states and energy constraints in the model configuration and energy budget analysis in the future work.

On the other hand, although *in situ* observations of the vertical profiles of temperature and salinity are used here for the validation of the estimation based on tidal energetics, these observations are only available in very limited areas of the AS. The accuracy and applicability of the fine-scale parameterization of turbulence remain a topic of debate in the community. As such, direct measurements of small-scale turbulence with microstructure profilers, as well as more full-depth temperature/salinity profiles in the deep basin of the AS, are needed for a more comprehensive validation of our internal tide energetics based estimates of the tidal dissipation and mixing in the AS.

## Appendix A: Sensitivity of the diapycnal diffusivities to the mixing efficiency Γ as well as the associated parameters $\Gamma^*$ and $Re_b^*$ in Equation 5

The estimations of diapycnal diffusivities using different values of Γ as well as the associated parameters $\Gamma^*$ and $Re_b^*$ in Equation 5 are shown in Figure A1. When Γ is taken as a function of the buoyancy Reynolds number, the estimated diapycnal diffusivities near the bottom of the entire AS basin are of $O\left(10^{-4}-10^{-3}\right)$ and $O\left(10^{-3}-10^{-2}\right)$ with the lower bounds ($\Gamma^*=0.2$, $Re_b^*=100$) (Figures A1a and A1e) and the upper bounds ($\Gamma^*=0.5$, $Re_b^*=300$) (Figures A1b and A1f) as suggested by Mashayek et al. (2017); when Γ is taken as a constant value of 0.2, the estimated diapycnal diffusivities of $O\left(10^{-2}-10^{-1}\right)$ m$^2$ s$^{-1}$ occur near the bottom of the entire AS basin (Figures A1c and A1g), which is 1–2 orders of magnitude larger than the estimation of those taking Γ as a function of the buoyancy Reynolds number. Therefore, the use of a constant Γ of 0.2 generally overestimates diapycnal mixing in the deep ocean where the stratification is quite weak. A much smaller value of Γ (e.g., 0.02, Figures A1d and A1h) would give similar values of diapycnal diffusivities, but will not resolve the spatial variability.

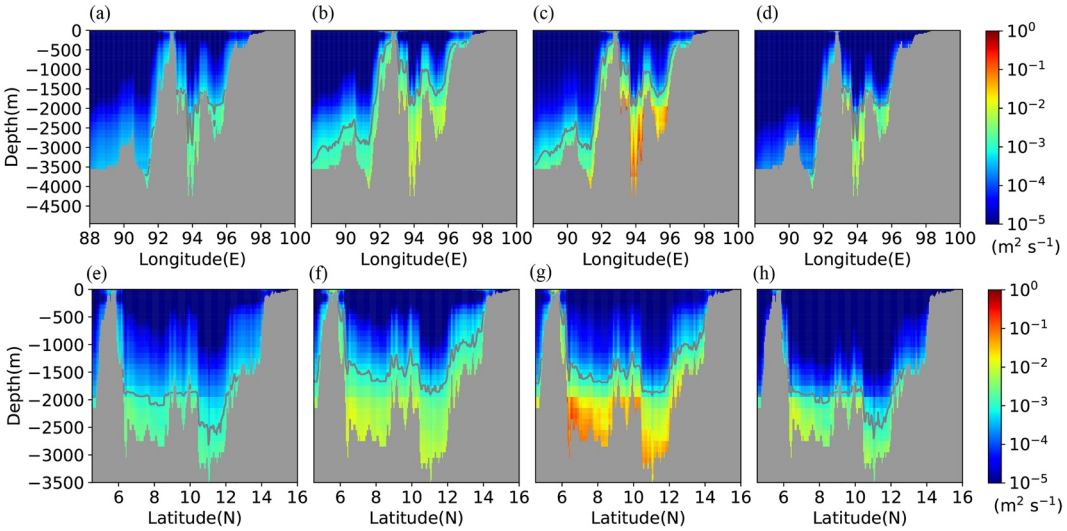


**Figure A1.** Cross-sectional distributions of diapycnal diffusivities with Γ that is a function of the buoyancy Reynolds number with (a and e) the lower bounds (Γ* = 0.2, $Re_b$* = 100) and (b and f) the upper bounds (Γ* = 0.5, $Re_b$* = 300) (c and g) Γ = 0.2, and (e and h) Γ = 0.02 along (a–d) 9.2°N and (e–h) 95°E.

**Table A1**
*Baroclinic Energy Budget Analysis for Different Regions (A, B, C, and D) in the Andaman Sea for the Two Experiments With Different Vertical Resolutions*

| Unit(GW) | | A | B | C | D |
|---|---|---|---|---|---|
| Barotropic-to-baroclinic | 58 layer | 2.70 | 11.86 | 4.91 | 4.54 |
| Conversion | 115 layer | 2.78 | 12.11 | 4.87 | 4.64 |
| | Difference | +2.96% | +2.11% | −0.81% | +2.20% |
| Baroclinic energy | 58 layer | 1.85 | 5.05 | 1.60 | −0.41 |
| Flux divergence | 115 layer | 1.94 | 5.41 | 1.71 | −0.44 |
| | Difference | +4.86% | +7.13% | +6.88% | +7.32% |
| Dissipation | 58 layer | 0.85 | 6.81 | 3.31 | 4.95 |
| | 115 layer | 0.84 | 6.70 | 3.16 | 5.08 |
| | Difference | −1.18% | −1.62% | −4.53% | +2.63% |

**Table A2**
*Baroclinic Energy Budget Analysis for Different Regions (A, B, C, and D) in the Andaman Sea for the Two Experiments With Different Horizontal Resolutions*

| Unit(GW) | | A | B | C | D |
|---|---|---|---|---|---|
| Barotropic-to-baroclinic | 1/24° | 2.70 | 11.86 | 4.91 | 4.54 |
| Conversion | 1/48° | 2.69 | 13.76 | 5.34 | 4.49 |
| | Difference | −0.37% | +16.02% | +8.76% | −1.10% |
| Baroclinic energy | 1/24° | 1.85 | 5.05 | 1.60 | −0.41 |
| Flux divergence | 1/48° | 1.81 | 5.62 | 1.75 | −0.76 |
| | Difference | −2.16% | +11.29% | +8.57% | +85.37% |
| Dissipation | 1/24° | 0.85 | 6.81 | 3.31 | 4.95 |
| | 1/48° | 0.88 | 8.14 | 3.59 | 5.25 |
| | Difference | +3.53% | +19.53% | +8.46% | +6.06% |

## Appendix B: Sensitivity of the internal tide energy to model resolutions

To see how large the impact of horizontal and vertical resolutions on the diagnostic calculations is, we carry out two additional experiments with a higher vertical resolution of 115 layers and horizontal resolution of 1/48°×1/48°, respectively. Tables A1 and A2 compare energy diagnostics with those from the simulation using a vertical resolution of 58 layers and a horizontal resolution of 1/24°×1/24°. It can be seen that the changes due to the increase in vertical resolution do not exceed 8%. In addition, for the experiment with horizontal resolution of 1/48°×1/48°, although the baroclinic energy flux divergence increases up to 85% in region D, its magnitude is an order lower than that of the barotropic-to-baroclinic conversion, which results in a very small change in the dissipation rate (∼6%); the change of each terms in regions A, B, and C due to the increase in horizontal resolution does not exceed 20%. Therefore, the experiment with vertical resolution of 58 layers and horizontal resolution of 1/24°×1/24° is acceptable and thus is adopted in this study under the consideration of saving computing resources.

## Data Availability Statement

The GEBCO_14 data are available at http://www.gebco.net/, GDEMv3 data are available at http://www.usgodae.org/pub/outgoing/static/ocn/gdem/, and OTIS data are available at http://volkov.oce.orst.edu/tides/YS.html.

**Acknowledgments**
This work was jointly supported by the Major Projects of National Natural Science Foundation of China (41931182, 41521005), Guangdong Key Project (2019BT02H594), National Natural Science Foundation of China (41676016 and 41976023), the Key Special Project for Introduced Talents Team of Southern Marine Science and Engineering Guangdong Laboratory (Guangzhou) (GML2019ZD0303). Z. L.'s participation of this work was supported by the National Natural Science Foundation of China (91858201 and 41622601) and the National Key R&D Program of China (2016YFC1401404). The authors gratefully acknowledge the use of the HPCC at the South China Sea Institute of Oceanology, Chinese Academy of Sciences. This work is also supported by Intergovernmental Oceanographic Commission (IOC) Sub-Commission for the Western Pacific (WESTPAC) through its project Monsoon Onset Monitoring and its Social and Ecosystem Impacts (MOMSEI). The AS cruises were supported by the China-Thailand Joint Laboratory for Climate and Marine Ecosystem. We are grateful for the CTD data provided by Joint cruise in the AS implemented by the First Institute of Oceanography (FIO), Ministry of Natural Resources, China and the Phuket Marine Biological Center (PMBC), Department of Marine and Coastal Resources, Thailand, available at ftp://210.77.90.150/pub/obs/.

## References

Buijsman, M. C., Klymak, J. M., Legg, S., Alford, M. H., Farmer, D., MacKinnon, J. A., et al. (2014). Three-dimensional double-ridge internal tide resonance in Luzon Strait. *Journal of Physical Oceanography*, *44*, 850–869. https://doi.org/10.1175/jpo-d-13-024.1

Buijsman, M. C., Legg, S., & Klymak, J. M. (2012). Double-ridge internal tide interference and its effect on dissipation in Luzon Strait. *Journal of Physical Oceanography*, *42*, 1337–1356. https://doi.org/10.1175/jpo-d-11-0210.1

Carter, G. S., Fringer, O. B., & Zaron, E. D. (2012). Regional models of internal tides. *Oceanography*, *25*, 56–65. https://doi.org/10.5670/oceanog.2012.42

Carter, G. S., & Gregg, M. C. (2002). Intense, variable mixing near the head of Monterey submarine canyon. *Journal of Physical Oceanography*, *32*, 3145–3165. https://doi.org/10.1175/1520-0485(2002)032<3145:ivmnth>2.0.co;2

Duda, T. F., & Rainville, L. (2008). Diurnal and semidiurnal internal tide energy flux at a continental slope in the South China Sea. *Journal of Geophysical Research*, *113*, C03025. https://doi.org/10.1029/2007jc004418

Egbert, G. D., Bennett, A. F., & Foreman, M. G. G. (1994). TOPEX/POSEIDON tides estimated using a global inverse model. *Journal of Geophysical Research*, *99*, 24821–24852. https://doi.org/10.1029/94jc01894

Egbert, G. D., & Erofeeva, S. Y. (2002). Efficient inverse modeling of barotropic ocean tides. *Journal of Atmospheric and Oceanic Technology*, *19*, 183–204. https://doi.org/10.1175/1520-0426(2002)019<0183:eimobo>2.0.co;2

Egbert, G. D., & Ray, R. D. (2000). Significant dissipation of tidal energy in the deep ocean inferred from satellite altimeter data. *Nature*, *405*, 775–778. https://doi.org/10.1038/35015531

Ferron, B., Mercier, H., Speer, K., Gargett, A. E., & Polzin, K. (1998). Mixing in the Romanche fracture zone. *Journal of Physical Oceanography*, *28*, 1929–1945. https://doi.org/10.1175/1520-0485(1998)028<1929:mitrfz>2.0.co;2

Gregg, M. C., D'Asaro, E. A., Riley, J. J., & Kunze, E. (2018). Mixing efficiency in the ocean. *Annual Review of Marine Science*, *10*(1), 443–473. https://doi.org/10.1146/annurev-marine-121916-063643

Hibiya, T., Furuichi, N., & Robertson, R. (2012). Assessment of fine-scale parameterizations of turbulent dissipation rates near mixing hotspots in the deep ocean. *Geophysical Research Letters*, *39*, L240601. https://doi.org/10.1029/2012GL054068

Jan, C., Chern, C. S., Wang, J., & Chiou, M. D. (2012). Generation and propagation of baroclinic tides modified by the Kuroshio in the Luzon Strait. *Journal of Geophysical Research*, *117*, C02019. https://doi.org/10.1029/2011JC007229

Jing, Z., Wu, L., Li, L., Liu, C., Liang, X., Chen, Z., et al. (2011). Turbulent diapycnal mixing in the subtropical northwestern Pacific: Spatial-seasonal variations and role of eddies. *Journal of Geophysical Research*, *116*, C10028. https://doi.org/10.1029/2011JC007142

Johns, W. E., Baringer, M. O., Beal, L. M., Cunningham, S. A., Kanzow, T., Bryden, H. L., et al. (2011). Continuous, array-based estimates of Atlantic Ocean heat transport at 26.5°N. *Journal of Climate*, *24*(10), 2429–2449. https://doi.org/10.1175/2010JCLI3997.1

Kang, D., & Fringer, O. (2012). Energetics of barotropic and baroclinic tides in the Monterey Bay area. *Journal of Physical Oceanography*, *42*, 272–290. https://doi.org/10.1175/jpo-d-11-039.1

Kelly, S. M., & Nash, J. D. (2010). Internal-tide generation and destruction by shoaling internal tides. *Geophysical Research Letters*, *37*, L23611. https://doi.org/10.1029/2010gl045598

Kerry, C. G., Powell, B. S., & Carter, G. S. (2013). Effects of remote generation sites on model estimates of $M_2$ internal tides in the Philippine Sea. *Journal of Physical Oceanography*, *43*, 187–204. https://doi.org/10.1175/JPO-D-12-081.1

Kerry, C. G., Powell, B. S., & Carter, G. S. (2014). The impact of subtidal circulation on internal tide generation and propagation in the Philippine Sea. *Journal of Physical Oceanography*, *44*, 1386–1405. https://doi.org/10.1175/JPO-D-13-0142.1

Klymak, J. M., Alford, M. H., Pinkel, R., Lien, R. C., Yang, Y. J., & Tang, T. Y. (2011). The breaking and scattering of the internal tide on a continental slope. *Journal of Physical Oceanography*, *41*, 926–945. https://doi.org/10.1175/2010jpo4500.1

Klymak, J. M., Simmons, H. L., Braznikov, D., Kelly, S. M., MacKinnon, J. A., Alford, M. H., et al. (2016). Reflection of linear internal tides from realistic topography: The Tasman continental slope. *Journal of Physical Oceanography*, *46*, 3321–3337. https://doi.org/10.1175/jpo-d-16-0061.1

Kostov, Y., Armour, K. C., & Marshall, J. (2014). Impact of the Atlantic meridional overturning circulation on ocean heat storage and transient climate change. *Geophysical Research Letters*, *41*(6), 2108–2116. https://doi.org/10.1002/2013gl058998

Kunze, E., Firing, E., Hummon, J. M., Chereskin, T. K., & Thurnherr, A. M. (2006). Global abyssal mixing inferred from lowered ADCP shear and CTD strain profiles. *Journal of Physical Oceanography*, *36*, 1553–1576. https://doi.org/10.1175/JPO2926.1

Kunze, E., & Toole, J. (1997). Tidally driven vorticity, diurnal shear, and turbulence atop Fieberling seamount. *Journal of Physical Oceanography*, *27*, 2663–2693. https://doi.org/10.1175/1520-0485(1997)027<2663:tdvdsa>2.0.co;2

Ledwell, J. R., Montgomery, E. T., Polzin, K. L., Laurent, L. C. S., Schmitt, R. W., & Toole, J. M. (2000). Evidence for enhanced mixing over rough topography in the abyssal ocean. *Nature*, *403*, 179–182. https://doi.org/10.1038/35003164

Ledwell, J. R., Watson, A. J., & Law, C. S. (1993). Evidence for slow mixing across the pycnocline from an open-ocean tracer-release experiment. *Nature*, *364*, 701–703. https://doi.org/10.1038/364701a0

Liu, Z. Y, Lian, Q., Zhang, F. T., Wang, L., Li, M.M, Bai, X. L., et al. (2017). Weak thermocline mixing in the North Pacific low-latitude western boundary current system. *Geophysical Research Letters*, *44*, 10530–10539. https://doi.org/10.1002/2017gl075210

MacKinnon, J., & Gregg, M. C. (2003). Mixing on the late summer New England Shelf – Solibores, shear, and stratification. *Journal of Physical Oceanography*, *33*, 1476–1492. https://doi.org/10.1175/1520-0485(2003)033,1476:MOTLNE.2.0.CO;210.1175/1520-0485(2003)033<1476:motlne>2.0.co;2

Marshall, J., Adcroft, A., Hill, C., Perelman, L., & Heisey, C. (1997). A finite-volume, incompressible Navier Stokes model for studies of the ocean on parallel computers. *Journal of Geophysical Research*, *102*, 5753–5766. https://doi.org/10.1029/96jc02775

Marshall, J., & Speer, K. (2012). Closure of the meridional overturning circulation through Southern Ocean upwelling. *Nature Geoscience*, *5*, 171–180. https://doi.org/10.1038/ngeo1391

Mashayek, A., Salehipour, H., Bouffard, D., Caulfield, C. P., Ferrari, R., Nikurashin, M., et al. (2017). Efficiency of turbulent mixing in the abyssal ocean circulation. *Geophysical Research Letters*, *44*, 6296–6306. https://doi.org/10.1002/2016GL072452

Mohanty, S., Rao, A. D., & Latha, G. (2018). Energetics of semidiurnal internal tides in the Andaman Sea. *Journal of Geophysical Research: Oceans*, *123*, 6224–6240. https://doi.org/10.1029/2018jc013852

Monismith, S., Koseff, J., & White, B. (2018). Mixing efficiency in the presence of stratification: When is it constant? *Geophysical Research Letters*, *45*(11), 5627–5634. https://doi.org/10.1029/2018gl077229

Munk, W. (1966). Abyssal recipes. *Deep Sea Research and Oceanographic Abstracts*, *13*(4), 707–730. https://doi.org/10.1016/0011-7471(66)90602-4

Munk, W., & Wunsch, C. (1998). Abyssal recipes II: Energetics of tidal and wind mixing. *Deep Sea Research*, *45*(12), 1977–2010. https://doi.org/10.1016/s0967-0637(98)00070-3

Murty, T. S., & Henry, R. F. (1983). Tides in the Bay of Bengal. *Journal of Geophysical Research*, *88*, 6069–6076. https://doi.org/10.1029/jc088ic10p06069

Nagai, T., & Hibiya, T. (2015). Internal tides and associated vertical mixing in the Indonesian Archipelago. *Journal of Geophysical Research: Oceans*, *120*, 3373–3390. https://doi.org/10.1002/2014JC010592

Nash, J. D., Alford, M. H., & Kunze, E. (2005). Estimating internal wave energy fluxes in the ocean. *Journal of Atmospheric and Oceanic Technology*, *22*, 1551–1570. https://doi.org/10.1175/jtech1784.1

Niwa, Y., & Hibiya, T. (2004). Three-dimensional numerical simulation of $M_2$ internal tides in the East China Sea. *Journal of Geophysical Research*, *109*, C04027. https://doi.org/10.1029/2003jc001923

Niwa, Y., & Hibiya, T. (2011). Estimation of baroclinic tide energy available for deep ocean mixing based on three-dimensional global numerical simulations. *Journal of Physical Oceanography*, *67*, 493–502. https://doi.org/10.1007/s10872-011-0052-1

Niwa, Y., & Hibiya, T. (2014). Generation of baroclinic tide energy in a global three-dimensional numerical model with different spatial grid resolutions. *Ocean Modelling*, *80*, 59–73. https://doi.org/10.1016/j.ocemod.2014.05.003

Osborn, T. R. (1980). Estimates of the local rate of vertical diffusion from dissipation measurements. *Journal of Physical Oceanography*, *10*, 83–89. https://doi.org/10.1175/1520-0485(1980)010<0083:eotlro>2.0.co;2

Osborne, A. R., & Burch, T. L. (1980). Internal solitons in the Andaman Sea. *Science*, *208*, 451–460. https://doi.org/10.1126/science.208.4443.451

Polzin, K. L., Na Garabato, A. C., Huussen, T. N., Sloyan, B. M., & Waterman, S. (2014). Finescale parameterizations of turbulent dissipation. *Journal of Geophysical Research: Oceans*, *119*, 1383–1419. https://doi.org/10.1002/2013jc008979

Polzin, K. L., Toole, J. M., Ledwell, J. R., & Schimitt, R. W. (1997). Spatial variability of turbulent mixing in the abyssal ocean. *Science*, *276*, 93–96. https://doi.org/10.1126/science.276.5309.93

Rahmstorf, S. (2003). Thermohaline circulation: The current climate. *Nature*, *421*, 699. https://doi.org/10.1038/421699a

Salehipour, H., Peltier, W. R., Whalen, C. B., & MacKinnon, J. A. (2016). A new characterization of the turbulent diapycnal diffusivities of mass and momentum in the ocean. *Geophysical Research Letters*, *43*(7), 3370–3379. https://doi.org/10.1002/2016gl068184

Sanchez-Franks, A., & Zhang, R. (2015). Impact of the Atlantic meridional overturning circulation on the decadal variability of the Gulf Stream path and regional chlorophyll and nutrient concentrations. *Geophysical Research Letters*, *42*, 9889–9897. https://doi.org/10.1002/2015GL066262

Scotti, A., & White, B. (2016). The mixing efficiency of stratified turbulent boundary layers. *Journal of Physical Oceanography*, *46*(10), 3181–3191. https://doi.org/10.1175/jpo-d-16-0095.1

Simmons, H. L., Jayne, S. R., Laurent, L. C. S., & Weaver, A. J. (2004). Tidally driven mixing in a numerical model of the ocean general circulation. *Ocean Modelling*, *6*, 245–263. https://doi.org/10.1016/s1463-5003(03)00011-8

St Laurent, L. C., Simmons, H. L., & Jayne, S. R. (2002). Estimating tidally driven mixing in the deep ocean. *Geophysical Research Letters*, *29*, 2106. https://doi.org/10.1029/2002gl015633

Talley, L. D. (2013). Closure of the global overturning circulation through the Indian, Pacific, and Southern Oceans: Schematics and transports. *Oceanography*, *26*, 80–97. https://doi.org/10.5670/oceanog.2013.07

Wang, X. W., Peng, S. Q., Liu, Z. Y., Huang, R. X., Qian, Y. K., & Li, Y. N. (2016). Tidal mixing in the South China Sea: An estimate based on the internal tide energetics. *Journal of Physical Oceanography*, *46*, 107–124. https://doi.org/10.1175/jpo-d-15-0082.1

Zilberman, N. V., Becker, J. M., Merrifield, M. A., & Carter, G. S. (2009). Model estimates of $M_2$ internal tide generation over Mid-Atlantic Ridge topography. *Journal of Physical Oceanography*, *39*, 2635. https://doi.org/10.1175/2008jpo4136.1